

## Sticking properties of ice grains

M. Jongmanns<sup>1,\*</sup>, M. Kumm<sup>1</sup>, G. Wurm<sup>1</sup>, D. E. Wolf<sup>1</sup>, and J. Teiser<sup>1</sup>

<sup>1</sup>University of Duisburg-Essen, D-47048 Duisburg, Germany

**Abstract.** We study the size dependence of pull-off forces of water ice in laboratory experiments and numerical simulations. To determine the pull-off force in our laboratory experiments, we use a liquid nitrogen cooled centrifuge. Depending on its rotation frequency, spherical ice grains detach due to the centrifugal force which is related to the adhesive properties. Numerical simulations are conducted by means of molecular dynamics simulations of hexagonal ice using a standard coarse-grained water potential. The pull-off force of a single contact between two spherical ice grains is measured due to strain controlled simulations. Both, the experimental study and the simulations reveal a dependence between the pull-off force and the (reduced) particle radii, which differ significantly from the linear dependence of common contact theories.

### 1 Introduction

In a standard scenario of planet formation, collisions between particles and aggregates thereof are important [1, 2]. Beyond the snowline in protoplanetary disks, water condenses into ice [3–5]. Therefore, collisions between ice particles occur. The interaction between these particles is fundamental for e.g. the formation of comets. Whether ice aggregates grow in mutual collisions depends on their sticking properties. It is commonly assumed [2], that ice aggregates can grow, if the kinetic collision  $E_C^{\text{coll}}$  energy does not exceed

$$E_C^{\text{coll}} = 0.4 \cdot F_C \delta_C. \quad (1)$$

Here,  $\delta_C$  is a critical displacement and  $F_C$  is the pull-off force needed to separate two particles. To understand the early process of planet formation, it is crucial to know the pull-off force  $F_C$ . Common contact theories (such as the JKR theory [6]) propose a linear dependence between  $F_C$  and the reduced radius  $R_{\text{red}} = \left(\frac{1}{R_1} + \frac{1}{R_2}\right)^{-1}$  ( $R_1$  and  $R_2$  being the radii of two contacting particles). However, it is not known if this dependence applies for values of  $R_{\text{red}}$  at the micro- or nanometer-scale for water ice. For example, in [7] Aumatell and Wurm investigated ice contacts at the nanometer-scale and found a big discrepancy between measured torques and those resulting from standard contact theories; in their work, the theoretical and experimental values differ up to a factor of 1000. To gain a better understanding of the critical pull-off force for small ice contacts, we have performed laboratory experiments (with micrometer ice particles, see section 2) and numerical simulations (with nanometer ice particles, see section 3). We compare the experimental and numerical results in section 4.

\*e-mail: Malte.Jongmanns@uni-due.de

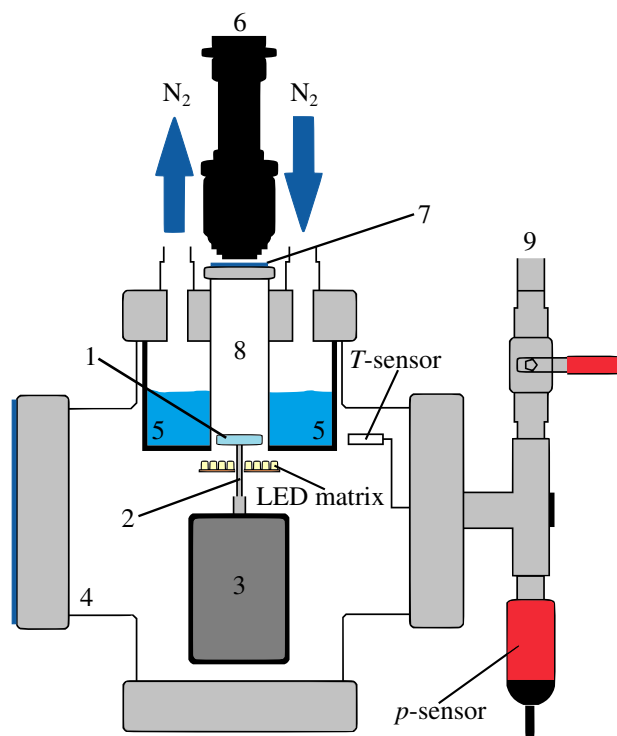


**Figure 1.** Our experimental setup as described in the text. (1): ice flywheel, (2): electric motor axis, (3): electric motor, (4): vacuum chamber, (5): liquid nitrogen-filled reservoir, (6): high-speed camera (not fully shown), (7): window, (8): cooling reservoir channel, (9): vacuum pump (not fully shown)

### 2 Experiment

Our experimental setup is shown in figure 1. A water ice flywheel (1) is mounted onto the axis (2) of an electric motor (3) and placed in the middle of a vacuum cham-

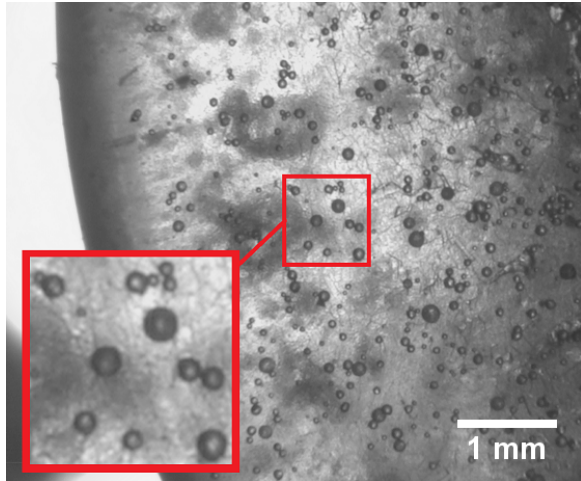


**Figure 2.** A snapshot of the flywheel taken by the highspeed camera. The inset shows ice grains on the surface of the ice flywheel in the static case (non-rotating) at higher resolution.

ber (4). A low temperature environment (of about  $-60^\circ\text{C}$ ) is provided by means of a liquid nitrogen-filled reservoir (5). Spherical water ice grains of an average size of  $(36.4 \pm 12.1) \mu\text{m}$  are brought onto the surface of the flywheel by spraying liquid water into the chamber (see figure 2). With the aid of a highspeed camera (6), it is possible to view the (spinning) ice flywheel through a window above the wheel (7). The view is along the channel of the cooling reservoir (8). The chamber is evacuated using a vacuum pump (9). Pressures of about  $p = 5 \times 10^{-2}$  mbar are reached within this process. Therefore, we examine experimentally hexagonal ice Ih.

The motor spins with a frequency  $\omega$ . We observed that, eventually (depending on  $\omega$ ), the ice grains are removed sideways from the flywheel because of a centrifugal force  $F_{\text{cf}} = m\omega^2 r_{\text{tr}}$ . Here,  $m$  is the mass of the ice grains and  $r_{\text{tr}}$  the distance from the rotation axis of a certain spherical ice particle. We calculate the mass by  $m = \frac{4}{3}\pi R^3 \cdot \rho_{\text{ice}}$  where  $\rho_{\text{ice}} = 925 \frac{\text{kg}}{\text{m}^3}$  [8] denotes the density of the ice and  $R$  the radius of the particle.

Due to the fact that the sticky spherical water ice particles were removed in the *tangential* direction from the surface of the ice flywheel, this process is linked to a critical torque  $M_C = R \cdot F_{\text{cf}}$ , where  $R = R_{\text{red}}$  is the radius of a certain spherical particle. We measure  $R$  by analyzing the highspeed camera images. Our measured data is shown in figure 3 in a  $M_C(R_{\text{red}})$ -plot. In this plot, our data points ( $\sim 100$ ) have been averaged by using a bin width  $\Delta R = 5 \mu\text{m}$ . The corresponding fit function of our raw data (without averaging) can well be described by a power law  $R_{\text{red}}^{3.34 \pm 0.40}$ . According to [2], there is a linear dependence between the critical torque  $M_C$  and the critical pull-off force  $F_C$ . Therefore, we obtain experimentally:

$$F_C^{\text{exp}} \propto R_{\text{red}}^{3.34 \pm 0.40} \quad (2)$$

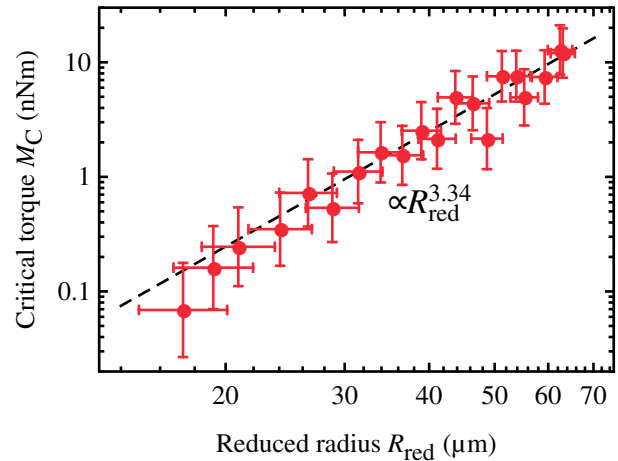


**Figure 3.** Measured  $M_C$  values on a log-log scale for averaged ice grain radii.

### 3 Simulations

In our second approach to study the sticking properties of ice contacts, we have performed molecular dynamics (MD) simulations. The simulations were carried out using a coarse-grained *model-Water(mW)*-potential [9] which proved successful in modeling ice [10]. All simulations were conducted in the canonical  $NVT$ -ensemble. The temperature  $T$  was controlled by means of the Nosé-Hoover chain thermostat [11]. An integration time step of  $\Delta t = 10$  fs was used and each system was relaxed for 0.3 ns.

The goal of our MD simulations is to calculate the pull-off force  $F_C$  for different ice contacts. This is achieved by conducting strain controlled simulations of specific configurations as will be described in the following. In our study, the ice contacts are modeled as two touching spherical ice grains. This is realized by placing mW-particles into a perfect hexagonal diamond lattice which is shaped as two touching half-spheres of the same radii  $R$ . By setting the lattice parameters to  $a = b = 4.51 \text{ \AA}$  and  $c = 7.34 \text{ \AA}$  [12], our diamond lattice corresponds to the structure of ice Ih at  $T = 223.15 \text{ K}$ . The crystal's  $\vec{a}$ -,  $\vec{b}$ - and  $\vec{c}$ -axis point in  $[2\bar{1}\bar{1}0]$ -,  $[\bar{1}2\bar{1}0]$ - and  $[0001]$ -direction, respectively. The configuration is enclosed by two walls which consist of the same lattice as the half-spheres. The walls are slightly bigger than the diameter of the spheres and as thick as two cutoff radii of the used potential. Such a start configuration is shown in figure 4 (a) for spheres of radii  $R/a = 14$ . The walls are needed for two reasons: first, to stabilize the configuration and second, to calculate the pull-off force  $F_C$  as it will be described in the next paragraphs. During the relaxation, the walls have the constraint, that they can only move (independently) “as a whole” in lateral direction. To implement this constraint, we neglect interactions of wall-particles among each other. After the relaxation, the positions of the walls are fixed to control the strain  $\epsilon$  of the configuration. Before the actual strain controlled simulations and the calculation of  $F_C$  are explained, we describe how the system evolves during its relaxation.

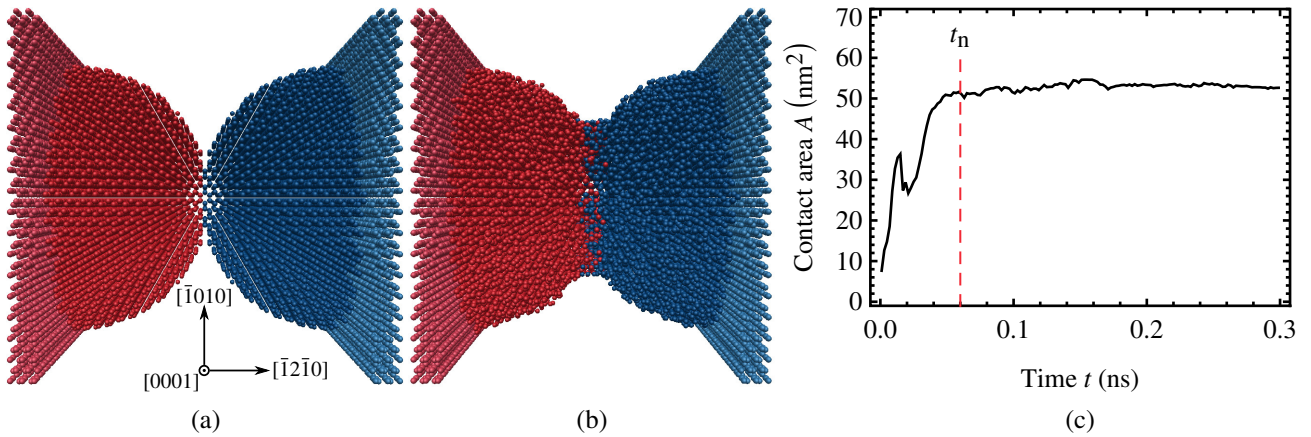


**Figure 4.** The geometry of the contact is modeled as two touching spheres (dark red and dark blue). (a) and (b) show the configuration for the specific case  $R/a = 14$  with the view on the (0001)-plane in each case. The walls are shown in lighter colors. (a) shows the initial system. (b) shows the system after its relaxation without any applied strain. Here it can be seen, that after the relaxation the contact is shaped as a neck. (c) shows the temporal evolution of the contact area  $A$  during the relaxation. The time  $t_n$  indicates the complete formation of the neck.

During the relaxation of the system, we investigated an attraction of both spheres due to van-der-Waals-interactions. This attraction ends after a time  $t_n$ , which is far smaller than the total relaxation time. At  $t_n$ , the contact between the two ice grains is shaped as a cylindrical neck and does not change its form for the remaining relaxation. In figure 4 (b), such a neck is shown for two spheres of radii  $R/a = 14$ . We examined the formation of the neck independently of  $R$ . To understand the formation of the neck in more detail, it is instructive to investigate a  $A(t)$ -plot. Here,  $A$  is the contact area between the two ice grains and is calculated by  $A = N_{cp}A_p$ .  $N_{cp}$  is the number of contacting mW-particle pairs and  $A_p$  their two-dimensional projected surface area [13]. To obtain  $N_{cp}$ , we count the mW-particle pairs at the grain contact whose distance is smaller than  $d = 3.3\text{\AA}$ . This value was calculated by means of a radial distribution function as it is described in detail in [13]. To obtain  $A_p$ , we assume the mW-particles to be perfect spheres with the volume of a water molecule  $V = 32.53\text{\AA}^3$  [8] and set  $A_p = \left(\frac{3}{4}\sqrt{\pi V}\right)^{2/3}$ . The temporal evolution of the calculated contact area during the relaxation is shown in figure 4 (c). As can be seen, the contact area at  $t = 0$  ns is not zero. This is due to the discrete nature of the particle system; it is not possible to initialize a lattice in such a way, that the two spheres only touch at one point. After  $t = t_n \approx 0.06$  ns (indicated by the dashed red line), the contact area stays constant for the remaining relaxation. At this point, the neck has been formed completely and does not change its size during the remaining relaxation; thus  $\frac{dA}{dt} \approx 0$  is measured. The contact area of a configuration is therefore the mean value of  $A$  measured between  $A(t = t_n)$  and  $A(t = 0.3$  ns).

After the relaxation, strain is imposed in  $\vec{x}$ -direction to measure  $F_C$  as follows: The right end of the left wall is  $x = 0$ . Then, after a time  $\tau = 0.1$  ns, we multiply the  $x$ -position of each mW-particle within the spheres by  $\lambda = 1.001$ . By doing this, the configuration is strained by 0.1% every  $\tau = 0.1$  ns, which defines a strain rate of

$\dot{\varepsilon} = 1 \times 10^{10} \text{ s}^{-1}$ . Every  $\tau$ , the position of the right wall is matched to the new length of the configuration. During the strain controlled simulations, the walls are fixed in their position. This allows us to measure the strain-force  $F_s$  which is needed to keep the configuration in its strained state:  $F_s$  is calculated by summing up all  $x$  components of the forces on all right wall-particles  $i$ :  $F_s = \sum_{i \in \text{r. wall}} f_{i,x}$ . The forces  $f_{i,x}$  on the right wall-particles arise due to interactions with the mW-particles of the right sphere. The value of  $F_s$  is calculated at each time step. This allows us to measure force-strain diagrams  $F_s(\varepsilon)$ . If we perform a full strain controlled simulation, the  $F_s(\varepsilon)$ -plot will have a maximum value at a critical strain  $\varepsilon_c$ . The pull-off force  $F_C$  is defined as  $F_C = F_s(\varepsilon_c)$ .

By changing the radii  $R$  of the spheres, the size of the contact neck changes. This allows us to measure a dependence between  $F_C$  and  $A$ . We have measured this dependence for various system parameters. For example, we have changed the strain rate  $\dot{\varepsilon}$ , the temperature  $T$ , the direction in which strain is imposed with respect to the crystal axes, the lattice orientation of each ice grain (which leads to a grain boundary at the contacting area) and the geometry of the contact. The change in the geometry of the contact is motivated by the cylindrical shape of the neck (see figure 4 (b)); thus, we have also modeled the contact as a cylinder with radius  $R_{cyl}$  and length  $L = 1.5R_{cyl}$ . A detailed analysis of all these system parameter dependencies will be given elsewhere. Here, we only give the main results. For all these different systems, we measured:  $F_C \propto A$ . Representative for all different systems, figure 5 shows a  $F_C(A)$ -plot for the following specific system:  $\dot{\varepsilon} = 1 \cdot 10^{10} \text{ s}^{-1}$ ,  $T = 223.15\text{K}$ , strain direction is along the crystal's  $[\bar{1}2\bar{1}0]$ -axis, no grain boundary and both contact geometries (with sphere radii of  $R/a = \{7, 8, 12, 13, 14, 15, 16, 18, 20\}$  and cylinder radii of  $R_{cyl}/a = \{4, 6, 8, 10, 12, 14\}$ ). The number of mW-particles vary in this specific study between  $N = 3698$  (smallest cylinder) and  $N = 121944$  (biggest spheres). Figure 5

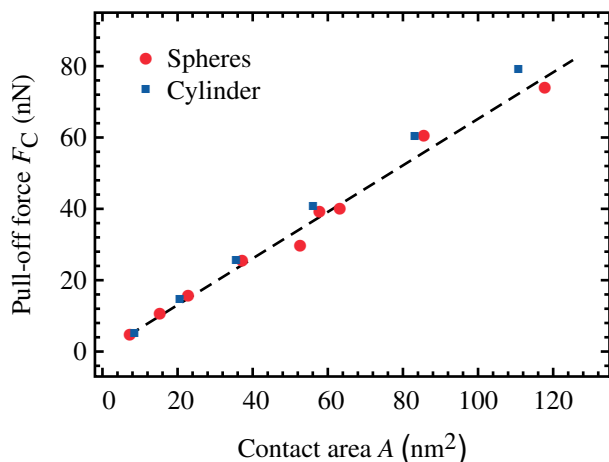


**Figure 5.** Measured  $F_C$  values as a function of the contact area  $A$  for both contact geometries. The black dashed line shows a linear fit for the sphere geometry.

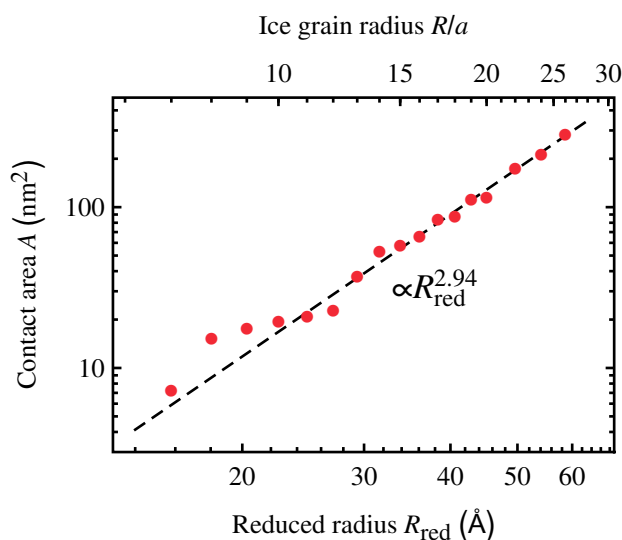


**Figure 6.** Measured  $A$  values on a log-log scale for different ice grain radii.

shows the already mentioned relation  $F_C \propto A$  and the fact, that the contact neck can be modeled as a cylinder (showing that the contact neck is indeed cylindrical).

To compare the simulated result with the experimental result, we have measured a dependence between the reduced ice grain radii  $R_{\text{red}}$  and the area  $A$  of the contact neck. Since the ice grains are both of the same size, the reduced radii are  $R_{\text{red}} = 0.5R$ . Figure 6 shows the  $A(R_{\text{red}})$ -plot on a log-log scale for the same system as mentioned above (with additional sphere radii up to  $R/a = 26$ , which corresponds to  $N = 256912$  mW-particles). The interesting result of the  $A(R_{\text{red}})$ -plot is:  $A \propto R_{\text{red}}^{2.94 \pm 0.073}$ . Since we

have always measured  $F_C \propto A$ , the result of the simulations is:

$$F_C^{\text{simul}} \propto R_{\text{red}}^{2.94 \pm 0.073} \quad (3)$$

## 4 Conclusions

The experimental and simulated results (equations 2 and 3) reveal a non-linear dependence between the pull-off force  $F_C$  and the reduced radii of the ice grains  $R_{\text{red}}$ . Both power laws are similar and match within the standard error. Our results differ so clearly from the common linear dependence [6], that we have to conclude, that ice grains at the nano- and micrometer-scale might not be described approximately by common contact theories. This has an interesting impact on the understanding of the early formation of e.g. icy planets, asteroids or comets: The pull-off force defines, whether particles are kept together after a collision. Therefore, our results reveal, that the growth of dust aggregates at the nano- and micrometer-scale might proceed differently than previously thought.

## References

- [1] J. Blum, G. Wurm, Annual Review of Astronomy and Astrophysics **46**, 21 (2008)
- [2] C. Dominik, A. Tielens, The Astrophysical Journal **480**, 647 (1997)
- [3] J.P. Williams, L.A. Cieza, Annual Review of Astronomy and Astrophysics **49**, 67 (2011)
- [4] H. Terada, A.T. Tokunaga, N. Kobayashi, N. Takato, Y. Hayano, H. Takami, The Astrophysical Journal **667**, 303 (2007)
- [5] M. Honda, A. Inoue, M. Fukagawa, A. Oka, T. Nakamoto, M. Ishii, H. Terada, N. Takato, H. Kawakita, Y. Okamoto et al., The Astrophysical Journal Letters **690**, L110 (2008)
- [6] K. Johnson, K. Kendall, A. Roberts, Proceedings of the Royal Society of London A: Mathematical, Physical and Engineering Sciences **324**, 301 (1971)
- [7] G. Aumatell, G. Wurm, Monthly Notices of the Royal Astronomical Society **437**, 690 (2014)
- [8] V.F. Petrenko, R.W. Whitworth, *Physics of ice* (OUP Oxford, 1999)
- [9] V. Molinero, E.B. Moore, The Journal of Physical Chemistry B **113**, 4008 (2008)
- [10] E.B. Moore, V. Molinero, Nature **479**, 506 (2011)
- [11] G.J. Martyna, M.L. Klein, M. Tuckerman, The Journal of chemical physics **97**, 2635 (1992)
- [12] K. Röttger, A. Endriss, J. Ihringer, S. Doyle, W. Kuhs, Acta Crystallographica Section B: Structural Science **50**, 644 (1994)
- [13] S. Solhjoo, A.I. Vakis, Computational Materials Science **109**, 172 (2015)